Cellulose (2021) 28:1469–1488
https://doi.org/10.1007/s10570-020-03606-8

ORIGINAL RESEARCH

TEMPO-oxidized cellulose nanofibers/polyacrylamide hybrid hydrogel with intrinsic self-recovery and shape memory properties

Ya Lu · Jingquan Han · Qinqin Ding · Yiying Yue · Changlei Xia · Shengbo Ge · Quyet Van Le · Xiaomin Dou · Christian Sonne · Su Shiung Lam

Received: 23 August 2020 / Accepted: 23 November 2020 / Published online: 6 January 2021

Abstract Shape memory hydrogels attract increasing attention due to their promising applications as intelligent biomaterials for actuators, biomedicine and sensory applications. Nonetheless, the integration of synergistic characteristics providing good mechanical properties and ideal self-recovery rate still remains a challenge. To tackle this, we develop a novel nanocomposite hydrogel by radical polymerization. TEMPO-oxidized cellulose nanofibers (TOCNs) with high strength and ultra-high aspect ratio were introduced to improve the energy dissipation mechanism and enhance the fatigue resistance of polyacrylamide (PAAM) hydrogel. Interestingly, the nanocomposite hydrogel displays unprecedented shape memory properties through coordination with Fe^{3+}. The resulting TOCN/PAAM hydrogel achieves excellent energy dissipation capability (9.68 MJ m^{-3} at 60% strain), satisfactory viscoelasticity (51.1 kPa) and good self-recovery rate (about 93.2% after 30 min recovery). In particular, the 3% TOCN/PAAM-Fe^{3+} hydrogel exhibits better tensile performance. This nanocomposite hydrogel with good shape memory properties and excellent mechanical strength has broad application prospects in soft actuators and sensory research.

Supplementary information The online version of this article (https://doi.org/10.1007/s10570-020-03606-8) contains supplementary material, which is available to authorized users.

Y. Lu · J. Han (✉) · Q. Ding · C. Xia (✉) · S. Ge · C. Sonne · S. S. Lam
College of Materials Science and Engineering, Joint International Research Lab of Lignocellulosic Functional Materials, Nanjing Forestry University, Nanjing 210037, People's Republic of China
e-mail: hjq@njfu.edu.cn

C. Xia
e-mail: changlei.xia@njfu.edu.cn

Y. Yue
College of Biology and Environment, Nanjing Forestry University, Nanjing 210037, People's Republic of China

Q. Van Le
Institute of Research and Development, Duy Tan University, Da Nang 550000, Vietnam

X. Dou
College of Environmental Science and Engineering, Beijing Forestry University, Beijing 100083, People's Republic of China

C. Sonne
Department of Bioscience, Arctic Research Centre (ARC), Aarhus University, Frederiksborgvej 399, PO Box 358, 4000 Roskilde, Denmark

S. S. Lam (✉)
Pyrolysis Technology Research Group, Institute of Tropical Aquaculture and Fisheries (AKUATROP) and Institute of Tropical Biodiversity and Sustainable Development (Bio-D Tropika), Universiti Malaysia Terengganu, 21030, Kuala Nerus, Terengganu, Malaysia
e-mail: lam@umt.edu.my

Graphic abstract

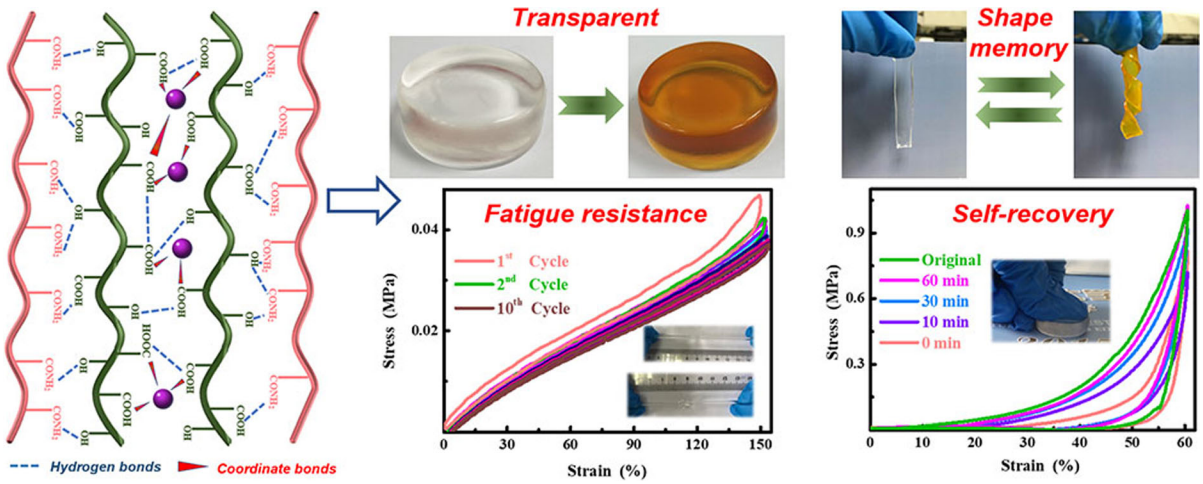

Keywords Shape memory hydrogels · Polyacrylamide · Nanocellulose · Mechanical properties

Introduction

"Smart" materials are defined as materials whose functions are changed in a controlled manner via adaption to the surrounding environment and/or their own state (Hu et al. 2012). These stimuli-responsive materials withstand changes in properties such as the material's shape, mechanical stiffness/flexibility, porosity, and opacity (Yang et al. 2020a). Due to these interesting characteristic changes, "smart" materials have great potential for application in many fields with medical domain being the most promoted (Qiu and Hu 2013). In particular, shape memory polymers (SMPs) are smart materials that rapidly developed over the past few years. SMPs can withstand and restore temporary deformation when exposed to specific external factors such as temperature change, light, solvent, moisture and electric fields (Li et al. 2017b; Liu et al. 2018).

Most studies on SMPs are limited to those made from dry state pure polymers. In recent years, we have witnessed a rapid growth in shape memory hydrogel (SMH), which is a swollen, 3D hydrophilic polymer network containing large amounts of water (Hu et al. 2015). SMHs have application prospects in many fields including tissue engineering, smart customer products, adaptive biomedical devices just to mention a few (Ma et al. 2018). However, most of the hydrogels exhibit poor mechanical properties at swollen state, which limits their further applications in many fields (Yuan et al. 2016). In recent years, hydrogels with improved mechanical properties have been fabricated including double network (DN), nanocomposite (NC) and dual cross-linked (DC) hydrogels (Hu et al. 2016; Shams Es-haghi and Weiss 2017). In particular, the mechanical properties of nanocomposite hydrogels could significantly be improved by adding reinforced organic/inorganic fillers such as clay, cellulose and carbon nanotubes (Han et al. 2018).

Inspired by increasing trends of recent years' environmental sustainability and protection, ecologically friendly composite hydrogels are increasingly synthesized from renewable natural resources (Han et al. 2014). Cellulose, regarded as a green biopolymer, attracts wide interests to be used as raw material for making advanced material due to its availability from a wide range of sources, exhibiting biodegradability, renewability, high Young's modulus and low density (Ge et al. 2020; Sun et al. 2015; Zhou et al. 2011). More importantly, cellulosic materials can be transformed into electronically conductive carbon materials with rich pore structure and high specific

surface area through a simple carbonization process. These characteristics make cellulosic materials suitable for use as smart materials and electronics. (Yang et al. 2020b; Zhao et al. 2020a, 2020b; Zheng et al. 2020) Comparing with cellulose, nano-cellulose has smaller size and diameter (1–100 nm in diameter and 100 nm to several micrometers in length), higher mechanical strength (elastic modulus of 130–150 GPa), larger specific surface area ($\sim$700 m^2/g) and lower thermal expansion (0.1 ppm K^{-1}). (Khalil et al. 2014; Song et al. 2013). Therefore, materials made of nanocellulose-based composite have excellent properties, which surpasses cellulose. Generally, nanocellulose is divided into cellulose nanocrystals (CNC), cellulose nanofibers (CNF) and bacterial cellulose (BC) (Niu et al. 2018).

Currently, polyacrylamide (PAAM) is widely used as the hydrogel matrix due to its non-toxicity, shape maintenance ability, mechanical strength, convenient adjustability of biophysical and chemical properties (Hynd et al. 2007; Lin et al. 2004). Conventionally cross-linked PAAM hydrogels are usually obtained by chemical polymerizing of AM monomers and crosslinkers under the action of an initiator. The gels are generally soft and brittle, have poor mechanical properties, and have difficulty in their withstanding of large deformations. Up to now, many studies have tried to improve the mechanical properties of PAAM gel by adding natural nanoscale fillers into the PAAM matrix unfortunately with limited success.

At present, the use of TEMPO (2,2,6,6-tetramethylpiperidine-1-oxyl radical)/NaBr/NaClO system for the purpose of oxidizing cellulose to obtain carboxylated nanocellulose has become a new research focus (Yue et al. 2019). The TEMPO oxidation method oxidizes a hydroxyl to aldehyde or carboxyl group on the cellulose molecular chain under oxidizing conditions thereby reducing the degree of polymerization to form nano-scale microcrystalline cellulose (Sheng et al. 2019). The method is simple to operate and the reaction can be carried out in an aqueous solution under mild conditions. The prepared nanocellulose surface has a large number of electron-donating functional groups, enabling a uniform and stable water dispersion (Saito et al. 2007). Yang et al. (2013) prepared a high-strength PAAM/CNC hydrogel with a core/shell structure with the silane-treated rod-shaped CNC acting as a multifunctional cross-linking agent to increase the viscoelasticity of the composite hydrogel. Chen et al. (2017) prepared CNF-enhanced PAAM nanocomposite hydrogel (PAAM/CNF) by in-situ polymerization of CNFs into PAAM hydrogel matrix, and found that the increase in mechanical strength of PAAM/CNF was mainly driven by the addition of CNF acting as a cross-linking agent and as a nano-reinforcing phase in the gel system. Yang and Xu (2017) prepared CNFs enhanced PAAM nanocomposite hydrogels (CNF-PAAM) through reversible hydrogen bonding and micro-covalent cross-linked PAAM matrix fusion forming a double crosslinked network with synergistically improved strength, Young's modulus and toughness. Zhou et al. (2011) reported the preparation of CNCs and then used it to enhance PAAM, using oscillatory shear on a rheometer to monitor the gelation process of the nanocomposite gels. Among the CNC content used, a 6.7 wt% load maximized the mechanical properties by almost 2.5-fold that of pure PAAM. In addition, BC composited PAAM hydrogels showed improved strength regardless of whether the BC existed in the form of cluster dispersion or interpenetration within the networks. (Velichko et al. 2017).

In this study, we successfully developed a type of TOCN/PAAM-Fe^{3+} hydrogels with intrinsic self-recovery and shape memory properties. A series of composite hydrogels with different TOCNs contents were investigated. We hypothesized that TOCN could act as a green nanocarrier to improve the brittleness network and dissipate energy that enhance the toughness of PAAM hydrogels. Due to the dynamic reversible nature of the hydrogen bonds, we postulated that the addition of TOCNs confer excellent mechanical property and self-recovery property of the TOCN/PAAM nanocomposite hydrogels following mechanical impact. With the addition of Fe^{3+}, the interaction between the carboxylic acid groups of TOCNs and Fe^{3+} is hypothesized to make the internal network of the hydrogel more densely crosslinked. Therefore, the presence of Fe^{3+} cations could effectively increase the stiffness and strength of the TOCN/PAAM composite hydrogel. The coordination of Fe^{3+} imparts a certain shape memory property to nanocomposite hydrogels, which greatly expands its application range.

Materials and methods

Materials

Bleached wood pulp (KC Flock, Tokyo, Japan) was purchased from Nippon Paper Chemicals Co. Acrylamide (AM) monomers, N,N′-methylenebis-acrylamide (NMBA), 2,2,6,6-tetramethylpiperidine-1-oxyl (TEMPO), initiator potassium persulfate (KPS), cross-linking accelerator N,N,N′,N′-tetramethylethylenediamine (TEMED), sodium hypochlorite (NaClO), sodium bromide (NaBr), potassium hydroxide (KOH) and Iron chloride hexahydrate ($FeCl_3{\cdot}6H_2O$) were obtained from Aladdin Industrial Inc. (Shanghai, China). All solutions were prepared using deionized water.

Preparation of TOCNs

TEMPO-mediated oxidation was conducted according to the procedure described in the literature. (Saito et al. 2006) Before preparation, the bleached wood pulp was dried at 45 °C for 24 h to remove residual moisture in the raw cellulose source. First, TEMPO (0.033 g) and NaBr (0.33 g) were sequentially dissolved in deionized water (400 mL), and thoroughly stirred at 10 °C to completely dissolve. Then, 10 g of dried wood pulp (mass fraction of about 20%) was added to the reaction system, and vigorously stirred to make it uniformly dispersed, then a certain amount of NaClO aqueous solution (15 mmol g^{-1} of cellulose weight) was added. The pH was controlled to about 10 by continuously dropping NaOH solution (0.5 M). After 6 h, the oxidized TOCN was filtered and washed several times with deionized water until suspension pH = 7. The oxidized TOCN was further dispersed in deionized water and ultrasonicated at 300 W for 15 min in an ice water bath to obtain the final TOCN colloidal suspension with a mass fraction of 0.82 wt%.

Fabrication of TOCN/PAAM hydrogel

TOCN/PAAM nanocomposite hydrogels were prepared by a free radical polymerization of AM monomers aqueous suspension of TOCNs. Initially, the concentration of AM was always controlled to 15.0 w/v%. Six gram of AM powder and NMBA (0.06 g, 1.0 wt% of AM) were dissolved in an aqueous suspension of TOCNs (0.06 g, 0.12 g and 0.18 g, 1.0, 2.0 and 3.0 wt% of AM), stirred vigorously for 1 h, and the oxygen in the mixed solution was removed in a nitrogen atmosphere for 10 min. The corresponding TOCN/PAAM hydrogels were labeled as 1% TOCN/PAAM, 2% TOCN/PAAM and 3% TOCN/PAAM, respectively. 2.5 mL KPS solution (20 mg mL^{-1}) and 30 μL TEMED were then added and stirred for 5 min. The bubbles in the mixed solution were removed under vacuum condition and then placed at 40 °C for 6 h to obtain TOCN/PAAM nanocomposite hydrogel. Our preliminary experiments found that the solution was too viscous when the TOCNs content exceeded 3 wt%, and the surface of the prepared composite hydrogels would be uneven (Fig. S1). Therefore, only 1–3 wt% of TOCNs were used for the experiment and in addition, a pure PAAM hydrogel without TOCNs was prepared as a blank control group according to the above procedure.

Fabrication of TOCN/PAAM-Fe^{3+} hybrid hydrogel

A straight hydrogel strip was obtained from the prepared 3% TOCN/PAAM hydrogel, and then immersed in a 0.2 M $FeCl_3$ solution. The corresponding gel system was subsequently named as TOCN/PAAM-Fe^{3+} hydrogel.

Characterization

The densities (ρ, g cm^{-3}) were determined from the volume (cm^3) and weight (g) of hydrogels. All samples (initial weight = W_o) were dried at 55 °C until obtained a constant weight (W_d). The water contents (W_c) were counted from Eq. (1):

$$W_c = \frac{W_0 - W_d}{W_0} \times 100\% \quad (1)$$

The prepared samples were completely soaked in deionized water at room temperature. The swollen hydrogels were weighed at set time intervals until a swelling equilibrium (W_{sw}) was reached. The hydrogel was then dried at 50 °C until constant weight (W_{dry}). The water swelling ratio (W_{sr}) was calculated from Eq. (2), and the equilibrium moisture content (E_m) was calculated from Eq. (3):

$$W_{sr} = \frac{W_{sw}}{W_0} \tag{2}$$

$$E_m = \frac{W_{sw} - W_{dry}}{W_{sw}} \times 100\% \tag{3}$$

The morphologies of hydrogels were examined by a field emission scanning electron microscopy (FE-SEM, JSM-7600F, JEOL Ltd., Japan). The transmission electron microscopy (TEM) images of TOCNs were obtained by a transmission electron microscope (JEM-1400, Japan Electronics Co., Ltd.). The optical absorption spectra of hydrogels were measured at wavelength from 200 to 800 nm using a UV − Vis spectrophotometer (UV-1780, Shimadzu Instruments Manufacturing Co., Ltd., China) at 25 °C. The absorption spectra were collected at a scan speed of 300 nm min^{-1} using deionized water as a reference. Fourier Transform Infrared Spectrometry (FTIR) analyses of all samples were performed in the range 4000–500 cm^{-1} using a VERTEX 80v spectrophotometer (Thermo Fisher Scientific Inc. USA).

For rheological measurements, the samples were subjected to frequency sweep and strain sweep tests using a HAAKE RheoStress 600 rheometer. Before the measurement, the dynamic strain sweep tests were performed from 0.1% to 100% at an angular frequency (ω) of 1.0 Hz. A strain (γ) was chosen to be 1.0% to ensure that the sample was deformed within the Linear Viscoelastic Region (LVR) in the following oscillation tests. The frequency sweep was performed within the linear viscoelastic behavior of the samples, controlling the magnitude and temperature of the strain, applying sinusoidal deformations of different frequencies, and testing at each frequency. The viscoelastic parameters included $G^{'}$ (storage modulus) and $G^{''}$ (loss modulus). The composite modulus (G^*) was calculated from Eq. (4), the composite viscosity (η^*) was calculated from Eq. (5):

$$G^* = \sqrt{G'^2 + G''^2} \tag{4}$$

$$\eta^* = \frac{G^*}{\omega} \tag{5}$$

For compression tests, the hydrogel samples (35 mm in diameter and 10 mm in height) were subjected to compressive stress (σ)–strain (ε) measurement using a universal testing machine (TY-8000B, China) at a compression speed of 15 mm min^{-1} at room temperature. When the normal stress reached the maximum load capacity (5 kN), the compression of all samples ended. The compressive elastic modulus (E) was calculated from the slope of the linear region of the stress–strain curve (ε_c = 5–15%). The energy dissipation (ΔU_i) was calculated using Eq. (6):

$$\Delta U_i = \int_{loading} \sigma d\varepsilon - \int_{unloading} \sigma d\varepsilon \tag{6}$$

The energy dissipation ratio (δ) was calculated as the following Eqs. (7) and (8) to measure how efficiently the sample dissipated energy:

$$\delta = \frac{\Delta U_i}{U_i} \tag{7}$$

$$U_i = \int_0^{\sigma_{max}} \sigma d\varepsilon \tag{8}$$

where U_i was the elastic energy stored in the samples when it was loaded elastically to the stress σ_{max} in the ith cycle.

In the self-recovery performance test, the samples were first compressed to a predetermined strain and then depressurized at the same speed. After each cycle of loading–unloading test, the samples were placed in a closed environment to minimize water evaporation and relaxed for a certain period (0–60 min) before proceeding to the next pressurization cycle. The self-recovery rate was defined as the ratio of energy consumption after different resting time to the initial cycle. For the fatigue resistance test, the stress was released immediately after the compression reached the set strain value, and immediately after the end of one cycle, the next cycle compression test was performed immediately. The σ-ε curve of the sample was observed after 10 consecutive loading–unloading cycles. The fatigue resistance of the composite hydrogels was characterized by 10 consecutive loading–unloading tests after standing for 24 h under sealed conditions.

The tensile stress–strain test was conducted at a fixed tensile speed of 30 mm min^{-1} using a universal testing machine (TY-8000B, China) equipped with a force sensor (50 N). The sizes of the samples were 4 mm in diameter and 25 mm in length. Toughness (T)

was calculated by the area under the stress–strain curves using following Eq. (9):

$$T = \int_{\varepsilon_0}^{\varepsilon_f} \sigma(\varepsilon) d\varepsilon \tag{9}$$

where ε_0 and ε_f corresponded to the initial stretch and fracture stretch, respectively.

The samples were first stretched to a predetermined strain (150%) at a speed of 30 mm min^{-1} and then depressurized at the same speed. The next cycle test was performed directly after each cycle. Tensile stress and energy dissipation changes were observed for 10 consecutive cycles. For the self-recovery test, the samples were allowed to relax for a specific waiting time before the next loading cycle, and the changes of various indexes before and after recovery were compared.

For examination of shape memory behavior, a straight hydrogel strip was cut from the prepared 3% TOCN/PAAM hydrogel, and the gel strip was twisted into a helical shape. To fix the temporary shape, the samples were immersed in an aqueous solution containing Fe^{3+}. The mechanical properties were adjusted by changing the immersion time (0–90 min) and tensile properties were tested.

Results and discussion

Fabrication process and synthesis mechanism of TOCN/PAAM-Fe^{3+} hybrid hydrogels

The fabrication process of the TOCN/PAAM-Fe^{3+} hydrogels is shown in Fig. 1a. First, the prepared TOCNs were dispersed in an aqueous solution to form a stable colloidal suspension with high transmittance. The AM monomers and the chemical crosslinkers NMBA were then added into the TOCNs suspension, while the KPS was used as a redox initiator in the grafting reaction of TOCNs as SO_4^- directly reacted with the polymer backbone of cellulose to form the necessary free radicals (Bhattacharya and Misra 2004). KPS and TEMED were added to the solution to induce "–OH" and "–COOH" groups on the surface of the TOCNs to generate free radicals and reacted with the double bond of the AM monomers to form a grafting point (covalent bond C–O) between the TOCNs and the PAAM chain (Ghosh et al. 1995; Zhou et al. 2011). At the same time, other free radicals presented in the solution initiated the homo-polymerization of AM to grow the PAAM macromolecular chain, while also forming a PAAM molecular chain under NMBA cross-linking. After that, a PAAM network containing TOCNs was formed. Finally, the

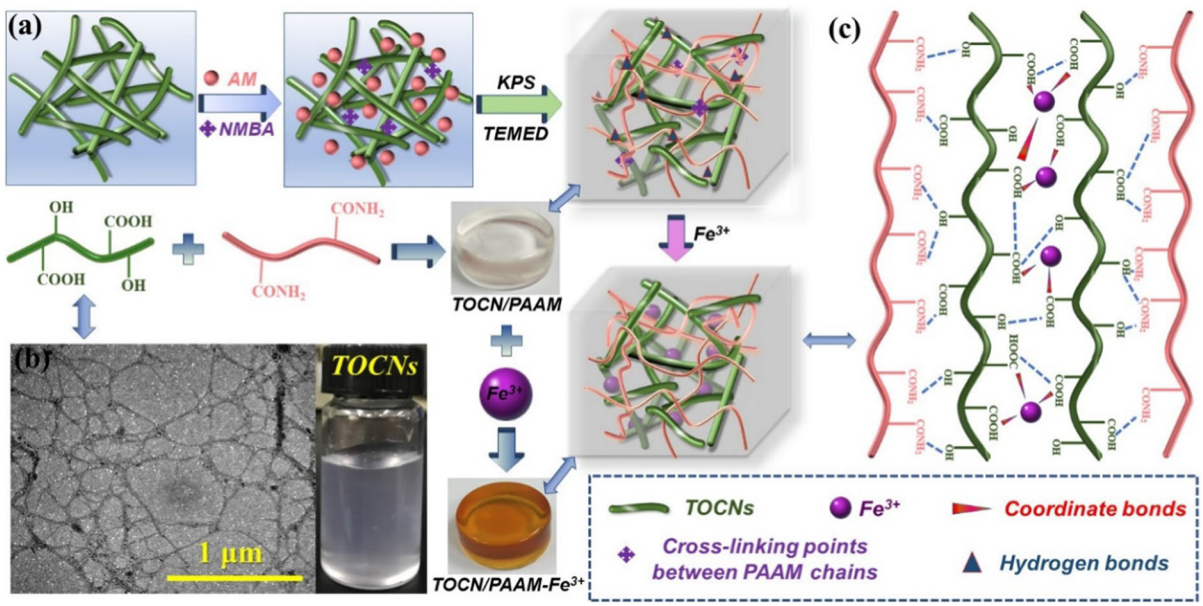

Fig. 1 **a** Synthesis process of TOCN/PAAM-Fe^{3+} hydrogels; **b** TEM image of TOCNs; **c** Formation mechanism of TOCN/PAAM-Fe^{3+} hydrogels

TOCN/PAAM hydrogels were soaked in $FeCl_3$ solution to obtain the TOCN/PAAM-Fe^{3+} hydrogels. The TEM image of TOCNs showed that the TOCNs fibers had an extremely long aspect ratio and an average length and diameter of 800 nm–1.0 μm and 5–10 nm, (Fig. 1b) being an ideal nanofiller. Figure 1c shows schematic illustration of 3D network formation of TOCN/PAAM-Fe^{3+} hydrogels. In addition to covalent bonding, dynamic hydrogen bonds were formed between PAAM and TOCNs. Combining transient (physical) cross-linking with a permanent (covalent) network that effectively adjusted the mechanical properties of the network in linear and nonlinearly deformed regions (Zhao 2014). The amide groups on PAAM chains interacted with hydroxyl and carboxyl groups on TOCN surfaces through hydrogen bonding. This powerful interaction facilitated physical adsorption of polymer chains onto the surface of TOCNs, forming an interfacial enhancement mechanism (Yang and Han 2016; Zhou et al. 2011). Fe^{3+} entering the internal hydrogel could form metal coordination interactions with –COOH groups of TOCNs, constituting a more compact network with enhanced mechanical strength.

Swelling behavior, transmittance and chemical analysis of Hybrid hydrogels

After soaking the prepared hydrogel in water, the swelling ratio of the PAAM and TOCN/PAAM nanocomposite hydrogels were measured at different durations (0–21 days) (Fig. 2a). In the first 5 days, the swelling rate of the hydrogels increased significantly and after 19 days, it reached a stable value. Compared with TOCN/PAAM composite hydrogels where the swelling ratio of the 1%, 2% and 3% TOCN/PAAM hydrogels were 4.10, 3.72 and 2.76 g g^{-1}, respectively, the swelling ratio of PAAM hydrogel (9.15 g g^{-1}) was much larger. In addition, the higher the TOCNs content of the TOCN/PAAM composite hydrogels, the lower the swelling ratio. As shown in Fig. 2b, the calculated equilibrium moisture content of the hydrogels decreased significantly with the increase of TOCN content. In hydrogel, the more clusters of TOCNs led to more hydrogen bonds formed inside the hydrogel and tighter crosslinks limiting the hydrogel swelling. The equilibrium moisture content of PAAM was about 96%, while that of 3% TOCN/PAAM was only 90%. Despite the increase of water content after equilibrium expansion, the volume of the 3% TOCN/

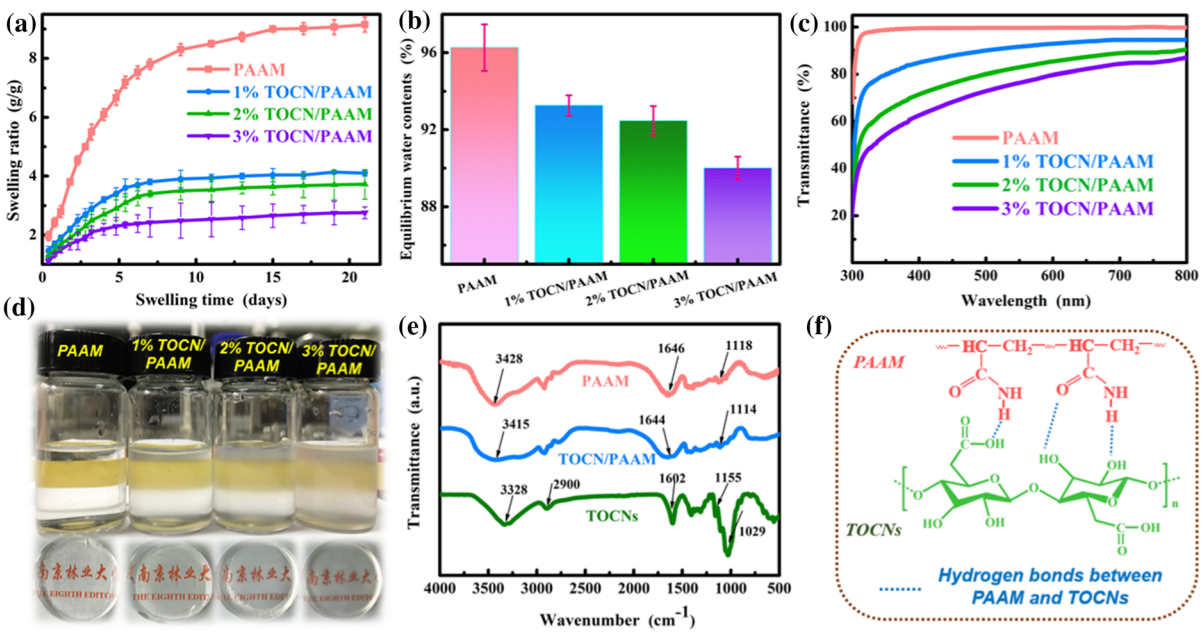

Fig. 2 **a** Swelling ratio of PAAM and TOCN/PAAM hydrogels with different contents of TOCNs; **b** equilibrium water contents of PAAM and TOCN/PAAM hydrogels; **c** UV–Vis transmittance spectra of PAAM, TOCN/PAAM and **d** photomacrograph of corresponding hydrogels; **e** FTIR spectra of TOCNs, PAAM, TOCN/PAAM and **f** interaction between PAAM and TOCNs

PAAM hydrogel remained relatively stable after 24 h revealing "non-expandable" properties when applied as a cartilage replacement material (Fig. S2) (Dai et al. 2015; Kamata et al. 2014). The swelling results also verified the existence of strong interaction between the PAAM chains and the TOCNs molecular cluster.

The UV–Vis spectra of PAAM and TOCN/PAAM in the wavelength range of 300–800 nm is shown in Fig. 2c. The pure PAAM hydrogel was almost transparent, and achieved an average transmittance of 99%. The introduction of nanocellulose reduced the transmittance of TOCNs-enhanced PAAM composite hydrogels because nanocellulose might block light. However, due to the high-water content and uniform network structure, TOCN/PAAM hydrogels still maintained high transparency. The visible light transmission was highly dependent on the quality and dispersion of the particles in the polymer system. The TOCNs formed a stable and uniform aqueous suspension colloid that was well dispersed in the hydrogel system, indicating excellent compatibility of the cellulose filler with the polymer matrix and allowing the hydrogel to reach translucent state (Yue et al. 2016). However, the refractive index of cellulose was greater than that of PAAM. Therefore, as the amount of TOCNs increased, the light scattering on the cellulose surface increased, and the transmittance of the composite hydrogels decreased. The transmittance test result was consistent with the macroscopic observation in Fig. 2d. In the ultraviolet region of 300–400 nm, the transmittance of TOCN/PAAM samples increased significantly with the increase of wavelength, suggesting that TOCNs had good absorption of ultraviolet light.

The chemical structure of TOCNs, PAAM and TOCN/PAAM hydrogels were characterized by FTIR as illustrated in Fig. 2e. The distinct broad characteristic peak near 3428 cm^{-1} belonged to N–H stretching vibration of PAAM (Li et al. 2017a), and the corresponding carbonyl group stretching vibration was detected near 1646 cm^{-1} (Kong et al. 2016). Another major absorption peak was detected at around 1118 cm^{-1}, which was attributed to the $–NH_2$ in-plane rocking vibration (Yuan et al. 2016). The main absorption peak of TOCNs shown around 3328 cm^{-1} was assigned to the stretching vibration of O–H on the cellulose molecular chains, which was the most important functional group in cellulose (Kamphunthong et al. 2012; Tang et al. 2019; Zuluaga et al. 2009). The absorption peak near 2900 cm^{-1} was due to the stretching vibration of the C–H group. Compared with cellulose, the TOCNs exhibited a stretching vibration peak of the sodium carboxylate group (–COONa) around 1602 cm^{-1}, implying the successful chemical oxidation of cellulose (Li et al. 2017b). Compared with pure PAAM hydrogel, the position of the peak of TOCN/PAAM nanocomposite hydrogels did not change significantly, probably because the characteristic absorption peak of TOCNs overlapped with the PAAM-related absorption peak. Besides, no new vibrational absorption peaks appeared on the TOCN/PAAM spectrum, indicating that no new chemical functional groups were formed between PAAM and TOCNs. The N–H stretching vibration absorption peak of PAAM significantly wider than the absorption peak of TOCN/PAAM, moving from 3428 cm^{-1} to 3415 cm^{-1}, which could be due to hydrogen bonds formed between PAAM and TOCNs. The intermolecular and/or intramolecular interactions between PAAM and TOCNs, such as hydrogen bonding or van der Waals forces, made the peak value of C=O stretching vibration of TOCN/PAAM hydrogels varying from 1646 cm^{-1} to 1644 cm^{-1} (Chen et al. 2017; Yan et al. 2017). Figure 2f shows a schematic diagram of hydrogen bonding between PAAM and TOCNs.

Dynamic viscoelasticity of hybrid hydrogels

The strain amplitude sweep tests of hydrogels were performed to confirm the LVR with the relation of curves for G' and γ presented in Fig. 3a. It could be seen that all four hydrogels exhibited a common hydrogel property (a quasi-solid with viscoelasticity), and G' was relatively stable within $\gamma = 1.0\%$. However, as the strain amplitude continued to increase, the G' of all hydrogels left their original linear level and exhibited nonlinear behavior, the strain at this time was called the critical strain point (γ_c). As the γ increased, the G' values of the hydrogels gradually decreased, indicating a transition from quasi-solid state to quasi-liquid state (Han et al. 2019). Therefore, the subsequent oscillation test was conducted within $\gamma = 1.0\%$ to ensure that the subsequent dynamic oscillation deformation of the composite hydrogel was within LVR. The G' of the TOCN/PAAM hydrogels was significantly larger than that of PAAM hydrogel, and the more TOCNs added, the greater the

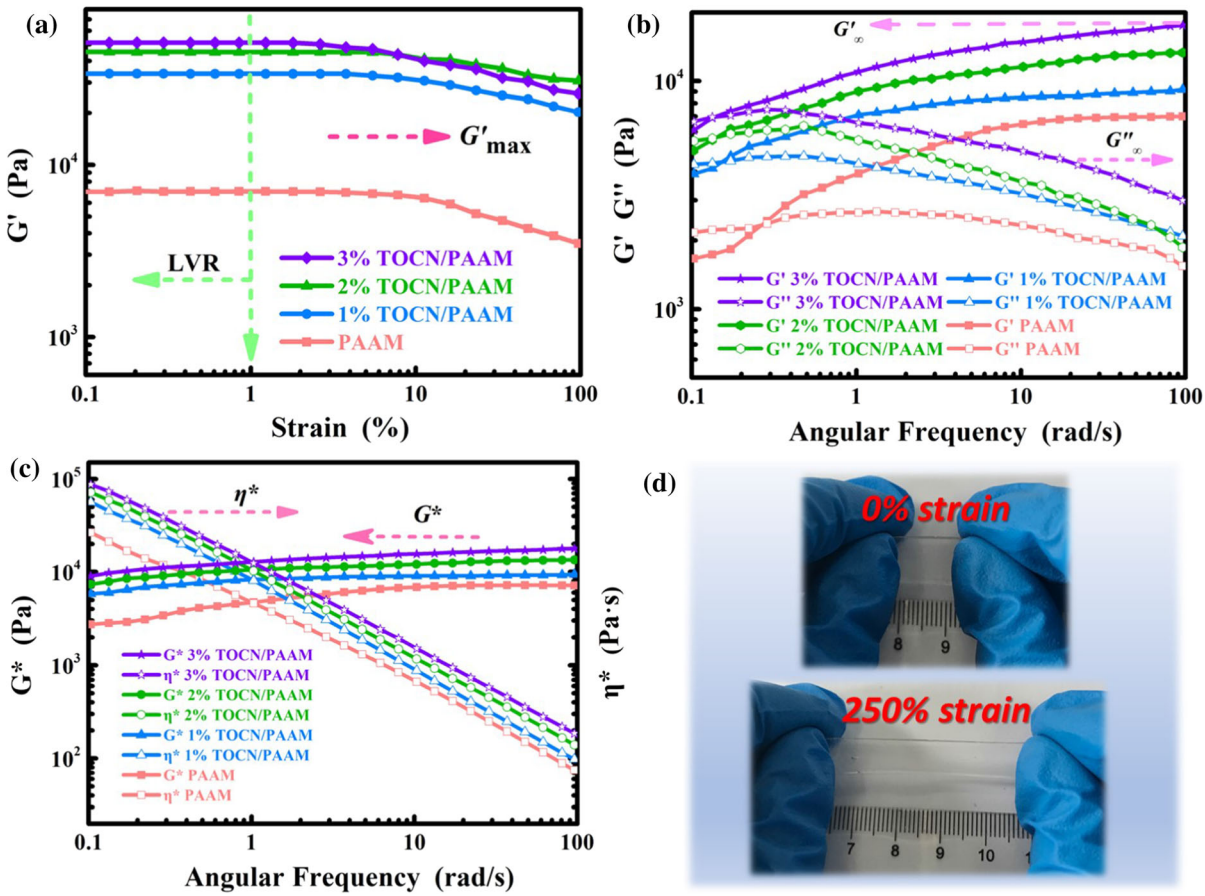

Fig. 3 Dynamic viscoelastic properties at 25 °C: **a** G' curves versus strain (ω = 1.0 Hz); **b** G' and G'' curves versus ω (1.0–100 Hz); **c** G^* and η^* curves (ω = 1.0 Hz); **d** 3% TOCN/PAAM hydrogel being stretched from 0 to 250% strain

Table 1 Rheological characteristics of hydrogels

Hydrogel	G'_∞ (kPa)	G''_m (kPa)	γ_c (%)	G'_{max} (kPa)
PAAM	7.0	2.6	7.8	7.0
1% TOCN/PAAM	9.2	4.7	3.8	33.8
2% TOCN/PAAM	13.3	6.1	2.6	45.2
3% TOCN/PAAM	17.6	7.5	1.8	51.1

viscoelasticity of the composite hydrogels. The G'_{max} of 3% TOCN/PAAM hydrogels (51.1 kPa) was about 7 times that of PAAM (7.0 kPa) (Table 1). Normally, the LVR became shorter as the sample approached the solid state. Comparing the 1% to 3% TOCN/PAAM and PAAM hydrogel samples, the larger the value of G'_{max} and the smaller the γ_c of the samples. Therefore, the viscoelasticity of the 3% TOCN/PAAM hydrogel was the most and the viscoelasticity of the pure PAAM hydrogel the least functional with a sevenfold difference. This showed that the addition of TOCNs could significantly enhance the viscoelasticity and mechanical strength of the hydrogels.

The G' and G'' of PAAM and TOCN/PAAM hydrogels within LVR are shown in Fig. 3b. As ω increased, G' gradually approached G'' and $G' = G''$, indicating that the hydrogel network was established (Wang and Chen 2011). After the hydrogel point, G' was still gradually increasing and G'' was gradually decreasing, indicating that the hydrogels were more and more elastic. Both TOCN/PAAM and PAAM hydrogels exhibited gelation characteristics, proving all hydrogels being viscoelastic materials. In addition, the intersection of TOCN/PAAM composite hydrogel was lower than PAAM hydrogel in the range of ω,

indicating that the TOCN/PAAM composite hydrogel exhibited more elastic properties.

By comparison, the $G^{'}$ of TOCN/PAAM composite hydrogels gradually increased with the addition of TOCNs, and $G^{'}_{\infty}$ of 3% TOCN/PAAM (17.6 kPa) being 2.5 times that of PAAM (7.0 kPa) which indicated that the more TOCNs the stronger the interaction between TOCNs and PAAM, and the higher the crosslinking density. The storage modulus of hydrogels increased with the addition of nanocellulose, which could be explained by physical entanglement and chemical crosslinking that had a great influence on the viscoelastic behavior (Han et al. 2014). Therefore, adding TOCNs significantly improved the mechanical strength of the hydrogels. With the increase of TOCNs, $G^{''}_{m}$ also gradually increased without a downward trend indicating that the effective cross-linking degree and polymer entanglement of hydrogels was significantly improved with a more stable morphology (Ivanov et al. 2004). A sharper contrast of the hydrogels was provided by the curves of complex modulus (G^{*}) and complex viscosity (η^{*}) versus ω (Fig. 3c). Among them, 3% of TOCN/PAAM hydrogels had the highest G^{*} and η^{*}, further confirming that 3% TOCN/PAAM hydrogel was the best viscoelastic hydrogel in all samples. In Fig. 3d, a block of 3% TOCN/PAAM composite hydrogel was stretched to a thin film (250% strain), demonstrating the "rubber-like" extensibility of the hydrogel. This dynamic viscoelasticity test showed that TOCNs form effective cross-ling interactions with PAAM forming a stable network structure. Among them, 3% TOCN/PAAM hydrogel had the highest $G^{'}$, $G^{''}$, G^{*} and η^{*}, showing that the composite hydrogels had the best viscoelasticity under this ratio.

Compression behavior of hybrid hydrogels

The compressive stress–strain and energy absorption-strain plots of PAAM hydrogel and TOCN/PAAM composite hydrogels at different TOCN contents are shown in Fig. 4a, b. Comparing the mechanical properties with the nominal stress and energy absorption at an 80% strain level, showed that all TOCN/PAAM composite hydrogels withstood higher stress than the pure PAAM hydrogel. The mechanical properties of the TOCN/PAAM was further improved as the TOCN content increased from 1 to 3 wt%. The increase in slope of the compressive stress–strain curve indicated that nanocellulose had excellent reinforcement properties (Han et al. 2013). In Table 2, the stress of the 3% TOCN/PAAM composite hydrogel at 80% strain was about 2.4 MPa. The compressive strength of 3% TOCN/PAAM hydrogel was superior to that of the various hydrogels reported in previous literature, including F127AZO@β-CD-PAAM hydrogel (about 0.65 MPa at 80% strain) (Song et al. 2018), gelatin/PAAM/Laponite nanocomposite hydrogels (208.4 kPa at 90% strain) (Li et al. 2015) and PAAM/polyaniline hydrogel (breaks at a stress of 0.7 MPa) (Dai et al. 2010). Considering the actual density, the specific compressive stress (σ_s) of 3% TOCN/PAAM ($\sim$ 1.9 MPa cm^3 g^{-1}) was about 19 times that of pure PAAM hydrogel ($\sim$ 0.1 MPa cm^3 g^{-1}). The improvement in compression performance was attributed to the well-dispersed TOCNs in the PAAM matrix (Yang et al. 2014). At ε = 80%, the energy absorption (E_a) of 3% TOCN/PAAM hydrogel (42.5 kJ m^{-3}) was 30 times larger than for PAAM hydrogel (1.4 kJ m^{-3}), indicating a higher toughness and strength of the composite hydrogels given the lack of deformation.

The microstructure of pure PAAM and 3% TOCN/PAAM hydrogels are presented in Fig. 4c, d. The corresponding idealized 3D network structure are shown in Fig. 4e. All hydrogels exhibited idealized 3D network structure (porous structure), which was typical for hydrogel morphology (Chen et al. 2017). The pure PAAM hydrogel had a relatively smooth porous structure, while the TOCN/PAAM nanocomposite hydrogels exhibited a coarse porous network structure. The pore diameter of TOCN/PAAM hydrogels was smaller than that of pure PAAM hydrogel, which also confirmed the fact that the composite hydrogels had a lower equilibrium swelling ratio due to the correlation between water content and the pore diameter. The higher the water content of the swellable hydrogel, the larger the pore diameter of the lyophilized hydrogel. In addition, the pore distribution of the TOCN/PAAM composite hydrogels was more regular than that of the pure PAAM hydrogel, indicating that the polymer network of the TOCN/PAAM composite hydrogels were more stable and regular, avoiding the collapse of the gel network structure and the formation of irregular pores during freeze-drying. In general, the stable regular network structure distributed the stress load evenly in the polymer matrix to improve the mechanical properties

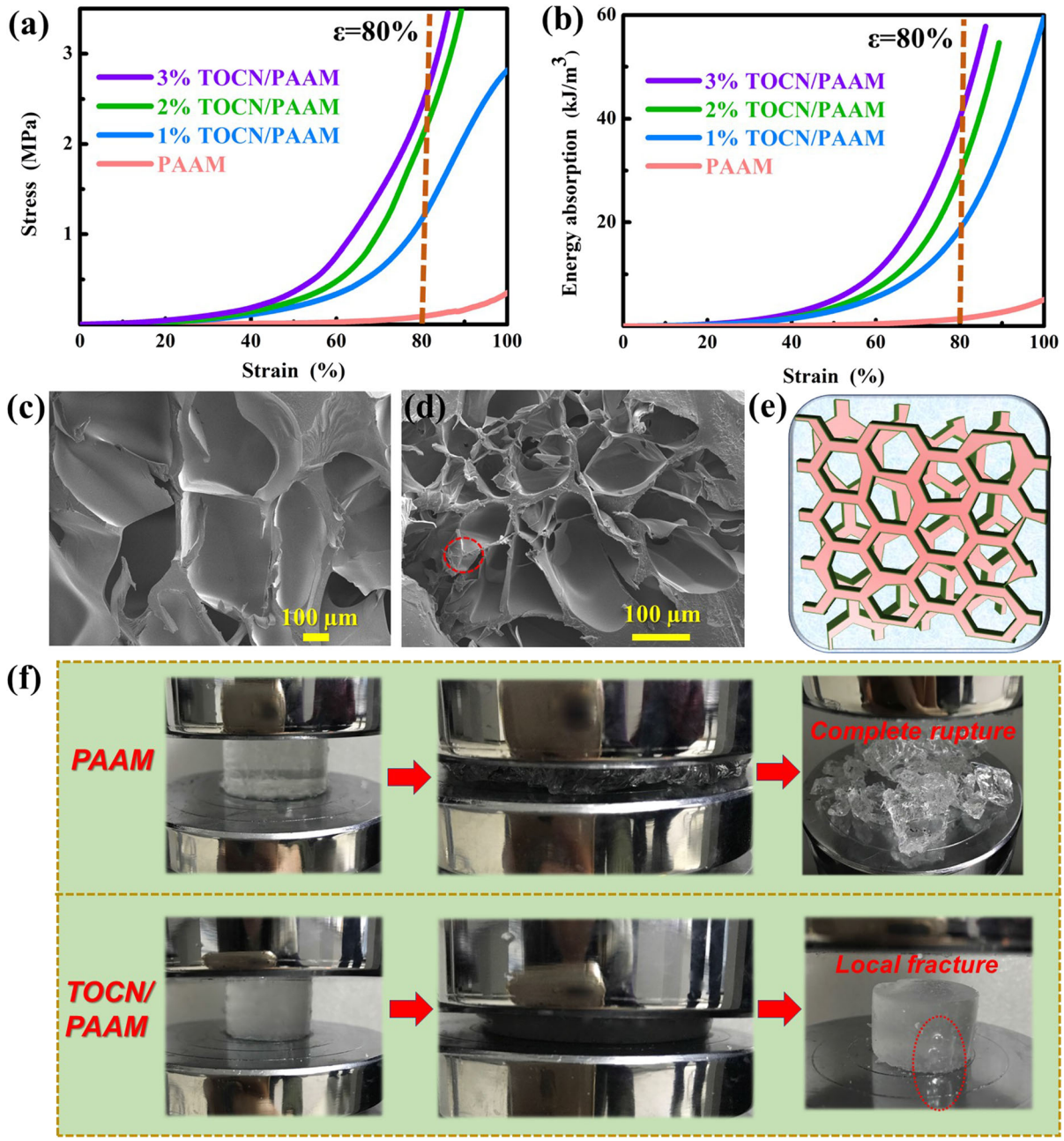

Fig. 4 **a** Compressive stress–strain plots and **b** energy absorption plots of PAAM and 1–3% TOCN/PAAM nanocomposite hydrogels; **c** SEM of pure PAAM hydrogel at a certain magnification (× 100); **d** SEM of 3% TOCN/PAAM hydrogel at a certain magnification (× 200); **e** proposed porous 3D network of TOCN/PAAM hydrogel; **f** comparison of fragmentation of PAAM and TOCN/PAAM composite hydrogels after compression

of hydrogels (Huang et al. 2007). As seen in Fig. 4d, some nanofibers were between the cavities of the pores of the 3% TOCN/PAAM hydrogels. In addition, a large number of TOCNs were found in the PAAM matrix indicating that the nanofibers could be pulled out during sample preparation likely ascribed to the large length and high flexibility of the TOCNs. This showed that TOCNs improved the mechanical properties of the hydrogels and reduced the swelling through strong hydrogen-bond interaction between

Table 2 Compression and physical properties of hydrogels

Hydrogel	σ (ε = 80%) (MPa)	E_a (ε = 80%) (kJ/m^3)	ρ (g/cm^3)	W_c (%)	σ_s (MPa cm^3/g)
PAAM	0.1 ± 0.0	1.4 ± 0.1	1.21 ± 0.10	89.6 ± 0.1	~ 0.1
1% TOCN/PAAM	1.2 ± 0.1	18.8 ± 0.1	1.23 ± 0.06	88.9 ± 0.1	~ 1.0
2% TOCN/PAAM	2.1 ± 0.1	29.6 ± 0.2	1.26 ± 0.07	88.2 ± 0.2	~ 1.6
3% TOCN/PAAM	2.4 ± 0.2	42.5 ± 0.3	1.28 ± 0.11	87.4 ± 0.1	~ 1.9

nanofibers and the PAAM matrix consistent with the test results of mechanical and swelling properties. When pure PAAM and 3% TOCN/PAAM hydrogel of same size are compressed, the pure PAAM hydrogel was completely broken while 3% TOCN/PAAM hydrogel had only local fracture (Fig. 4f). This clearly demonstrated that the composite hydrogels remained tough under high compressive stress and had excellent self-recovery properties.

The density (ρ) and water content (W_c) of the TOCN/PAAM hydrogels prepared by different ratios of TOCN are shown in Table 2. The average moisture content of the nanocomposite hydrogel was about 88.17%, and the mean ρ was about 1.26 g cm^{-3}. As the amount of TOCNs increased, the W_c of the hydrogels decreased and the ρ increased. Inside the PAAM hydrogels, molecular chains interdigitated to form a crosslinked network that accommodated water molecules result in a moisture content of up to 90%. With the addition of TOCNs, these molecules were intertwined with the PAAM network, thereby increasing the crosslink density of the hydrogel 3D network structure and the macroscopic density and mechanical strength. Simultaneously, the more the TOCNs added, the higher the crosslink density inside the hydrogel. As a result, the space for accommodating water molecules was occupied, which was specifically reflected in the W_c decrease.

The principle of toughened hydrogel was to introduce mechanical dissipation into the polymer network and hinder crack propagation (Zhao 2014). Figure 5a, b show the cyclic loading–unloading curves of pure PAAM and 1% ~ 3% TOCN/PAAM nanocomposite hydrogels at 60% compressive strain, as well as the corresponding compression elastic modulus and energy dissipation. In Fig. 5a, the TOCN/PAAM nanocomposite hydrogel exhibited greater hysteresis during the loading–unloading cycle compared to the pure PAAM hydrogel. With the TOCNs increasing, the hysteresis loop and the energy dissipation also increased, indicating that the TOCN/PAAM nanocomposite hydrogel consumed the applied energy more effectively when subjected to compression failure. This effective energy dissipation was mainly attributed to the high aspect ratio, high strength and excellent interfacial interaction with the matrix of the nanocellulose particles. This made the TOCNs load to transfer in a highly efficient energy dissipation manner enhancing the strength and toughness of the hydrogel composite (De France et al. 2017; Salas et al. 2014). The compressive elastic modulus of 3% TOCN/PAAM (220 kPa) was about twice that of pure PAAM (103 kPa) (Fig. 5b). As the TOCNs increased, the elastic modulus of the composite hydrogels increased accordingly. The results were consistent with the test results of compressive strength found in the energy dissipation data calculated by the hysteresis loop of Fig. 5a where the dissipated energy of 3% TOCN/PAAM (9.68 MJ m^{-3}) was about 14 times that of pure PAAM (0.67 MJ m^{-3}). This fully demonstrated the toughening effect of the TOCNs in PAAM hydrogel where the increase in the content led to more hydrogen bonding in the PAAM matrix giving the composite hydrogels a more pronounced mechanical strength.

Figure 5c, d show the cyclic loading–unloading curves of 3% TOCN/PAAM composite hydrogels under different compressive strains (30%, 40%, 50% and 60%), as well as the corresponding compression toughness and energy dissipation ratio chart. It could be seen from Fig. 5c that the loading–unloading curves of 3% TOCN/PAAM under different compressive strain conditions showed obvious hysteresis loops, indicating that the composite hydrogels could consume a high amount of energy in the cycle test. The hysteresis became more apparent when the compressive strain gradually increased to 60%. It can be seen from Fig. 5d that as the strain increased from 30 to 60%, the total compressive toughness of the composite hydrogels gradually increased, which could consume more energy and achieve higher energy dissipation

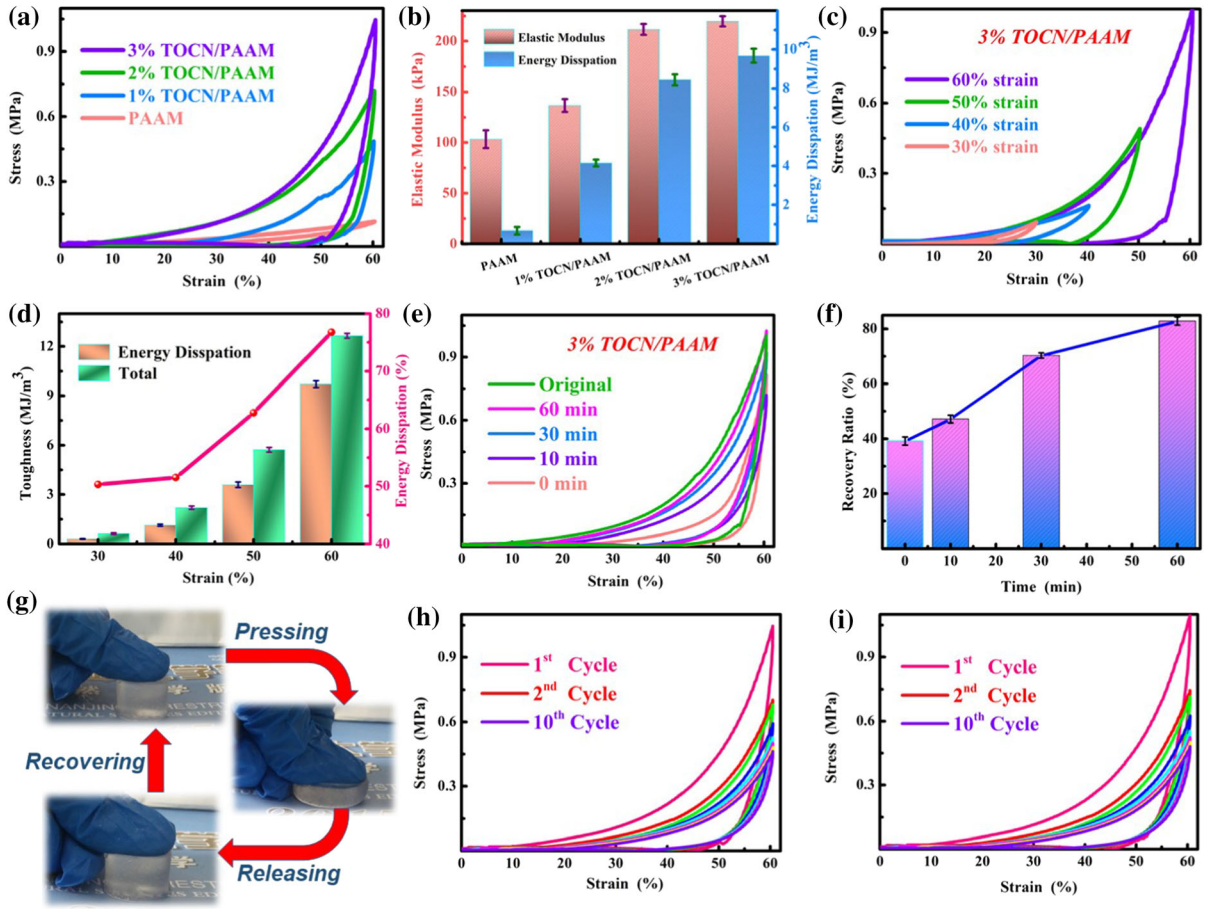

Fig. 5 **a** Cyclic compressive loading–unloading curves at 60% compressive strain of PAAM and 1% ∼ 3% TOCN/PAAM nanocomposite hydrogels; **b** compressive elastic modulus and corresponding energy dissipation at 60% strain of hydrogels; **c** cyclic loading–unloading curves and **d** toughness and energy dissipation ratio of 3% TOCN/PAAM hydrogel under different compressive strains (30%, 40%, 50%, 60%); **e** cyclic loading–unloading plots and **f** time-dependent recovery ratio of 3% TOCN/PAAM at 60% compressive strain with different resting times; **g** photographs revealing the notable compression resistance of 3% TOCN/PAAM hydrogel; fatigue resistance of the **h** as-prepared and **i** recovered 3% TOCN/PAAM hydrogels after 24 h resting time by ten consecutive loading–unloading cycles

rate. As the strain gradually increased, the chemical bonds between PAAM chains and TOCNs were partially broken to dissipate energy, while the synergy of weaker hydrogen bonds tended to break preferentially as sacrificial bonds to maximize energy dissipation. Therefore, the composite hydrogel could achieve higher energy dissipation efficiency as the strain increased during the cycle tests (Shao et al. 2017).

In addition to the significant increase in toughness and mechanical strength, the cross-linking network of TOCNs and PAAM was re-crosslinked and quickly recovered thereby giving the nanocomposite hydrogels excellent self-recovery abilities (Zhang et al. 2018). The cyclic loading–unloading curves of 3% TOCN/PAAM composite hydrogel at 60% compressive strain are shown in Fig. 5e with different rest times (0 ∼ 60 min) between two consecutive measurements. After the initial cycle measurement, the sample was re-tested after 0, 10, 30 and 60 min showing a self-recovery rate of 39.5%, 47.4%, 70.9%, and 82.1%, respectively (Fig. 5f). If the second compression cycle test was performed immediately after the first, the self-recovery effect of the composite hydrogel was very weak. With the extension of the rest time, the self-recovery degree gradually increased. Figure 5g shows the deformation process of a manually compression of 3% TOCN/PAAM hydrogel. Obviously, the hydrogel did not break under large

strain, which indicated that the 3% TOCN/PAAM conducting hydrogel had excellent compression resistance. In addition, after stress removal, 3% TOCN / PAAM composite hydrogel quickly returned to its original shape.

Owing to the excellent self-recovery properties, the composite hydrogels had high fatigue resistance following repeated deformation. Figure 5h shows 10 cycles of loading–unloading of 3% TOCN/PAAM composite hydrogel at 60% compression strain with no time interval between the two consecutive cycles. The hysteresis loop of the composite hydrogel and the maximum stress at 60% compressive strain were significantly reduced in the second cycle. This shows that the TOCNs network structure of the hydrogels underwent internal partial fracture and the fracture force could not be recovered immediately without breaking in the first cycle process of loading–unloading. However, the hysteresis loop and the maximum stress remained essentially unchanged after the fifth cycle, indicating that the 3% TOCN/PAAM composite hydrogel had good fatigue resistance. After standing for 24 h, another 10 consecutive cycles of loading–unloading test were performed on the self-recovering 3% TOCN/PAAM hydrogels (Fig. 5i). The fracture strength of the self-recovery composite hydrogels was even slightly higher than the initial value mainly due to the rearrangement of the TOCNs chain after cyclic loading increasing the physical crosslink density of the hydrogel, and the crosslinked network reconnected or recombined to form the optimal recombination to alleviate the internal stress of the hydrogel. The newly formed crosslinking network gave the TOCN/PAAM composite hydrogels excellent fatigue resistance showing that TOCN/PAAM hydrogels not only had good self-recovery ability but also had high fatigue resistance under cyclic loading (Shao et al. 2017).

Tensile behavior of hybrid hydrogels

Typical tensile stress–strain curves for PAAM and 1–3% TOCN/PAAM hydrogels is shown in Fig. 6a. The maximum tensile strength of pure PAAM hydrogel was about 0.02 MPa and in contrast, the tensile strengths of the hydrogels were enhanced by introducing TOCN, i.e., 1–3% TOCN/PAAM were 0.03, 0.05 and 0.07 MPa, respectively. With the increase of TOCNs content, the tensile strength also increased gradually. Moreover, the elongation at break of 2% TOCN/PAAM nanocomposite hydrogels was also greatly improved compared to pure PAAM (Fig. 6a). The improvement in tensile properties was mainly due to the hydrogen bonding between PAAM and TOCNs while the introduction of TOCNs cross-linking network helped to dissipate energy, withstand stress and reorganize the network after mechanical deformation, thereby significantly improving tensile and toughness. However, for covalently crosslinked hydrogels, the enhanced stiffness led to reduced stretchability and toughness (Semenov and Rubinstein 2002). Therefore, the more TOCNs added, the stronger the mechanical strength and the lower the elongation at break. The toughness of pure PAAM and 1–3% TOCN/PAAM hydrogels is shown in Fig. 6b. With the increase of TOCNs, the toughness of TOCN/PAAM composite hydrogels increased from 5.03 to 12.21 MJ m^{-3}, achieving a 6 times the toughness of the pure PAAM hydrogel (2.02 MJ m^{-3}), demonstrating the significant toughening effect of TOCNs on PAAM hydrogel. The enhancement of the mechanical properties of the TOCN/PAAM composite hydrogels was attributed to the addition of TOCNs filler, which transferred energy across the interface and resisted stress concentration to prevent the rupture from continuing to propagate inside the hydrogels (Hore and Composto 2013; Kumar et al. 2013). The TOCN/PAAM composite hydrogels could sustain various deformations including stretching and knotting (Fig. 6c, d). After the hydrogel was subjected to $\sim$ 100% tensile strain, the original shape restored instantly after removing the tensile force. The hydrogel still withstood a tensile strain of $\sim$ 250% after knotting, and quickly returned to the original state after releasing the strain, indicating that the TOCN/PAAM hydrogel had outstanding toughness and shape self-recovery properties.

A 3% TOCN/PAAM nanocomposite hydrogel was subjected to a cyclic tensile loading–unloading test at 150% tensile strain to measure recoverability of the mechanical properties of the composite hydrogels. Two consecutive cycles were tested at different intervals after the first cycle, where the loading–unloading measurement was repeated on the 3% TOCN/PAAM composite hydrogel after 0 min, 5 min and 30 min, respectively (Fig. 7a). A large hysteresis loop was observed in the first cycle, and the tensile stress and hysteresis of the composite hydrogel being significantly reduced when the second stretching was performed immediately. With the increase of rest

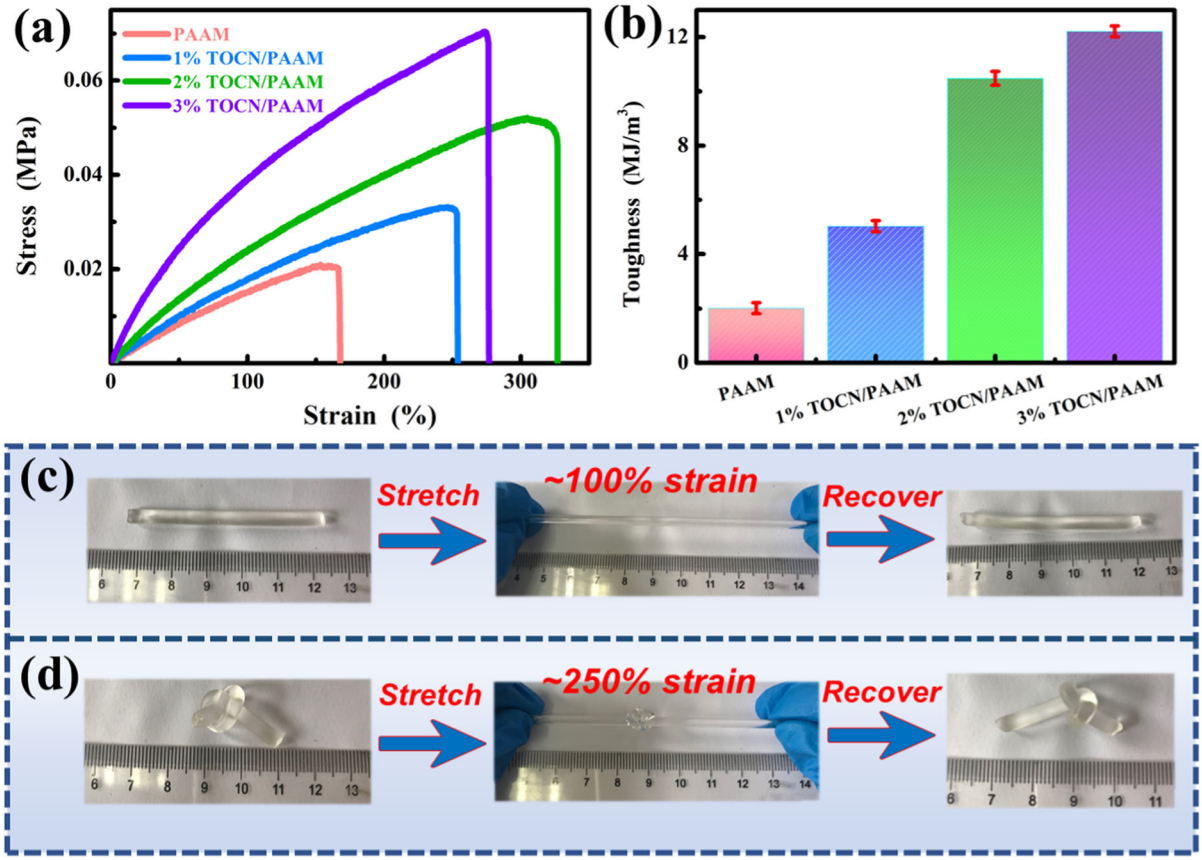

Fig. 6 **a** Tensile stress–strain curves of PAAM and 1% ∼ 3% TOCN/PAAM nanocomposite hydrogels, and **b** corresponding toughness of hydrogels; Photographs of 3% TOCN/PAAM hydrogels under different conditions: **c** ability to withstand stretching with ∼ 100% strain and recovery to its original length and shape; **d** ability to withstand stretching to ∼ 250% strain after knotting and recovery to its original state

time, the stress–strain curve gradually reverted to the original loading path. To evaluate the recovery efficiency, the self-recovery rate was measured in Fig. 7b. The results showed that when the rest time was 0 min, the self-recovery rate was only 33%, while after 30 min, it reached 93.2%. The self-recovery rate of as-prepared hydrogel was comparable to those of other previously reported hydrogels, including PAAAM gel (about 92% after 5 h recovery) (Zhang et al. 2017), PAAm-oxCNTs hydrogel (90.2% after the resting time of 20 min) (Sun et al. 2020) and HLP cross-linked hydrogels (completely recovered after resting for 10 min) (Xia et al. 2019). One of the most important properties for stretchable materials was reversible stretchability, and any minor irreversible deformation would ultimately compromise the overall stretchability of the material. The smaller the residual strain, the better the elastic reversibility of the material. As shown in Fig. 7b, the residual strain of the 3% TOCN/PAAM composite hydrogel gradually decreased with the extension of the standing time. After resting for 30 min, the residual strain was 2%. Even after the second cycle immediately after the first loading test, the residual strain of the composite hydrogel was only about 8.6%, which was mainly attributed to the elasticity generated by covalent crosslinking (Yang and Xu 2017).

The initial tensile cycle loading–unloading curves of 3% TOCN/PAAM composite hydrogel at 150% tensile strain and the curves measured again after resting for 24 h are shown in Fig. 7c. The corresponding graphs of changes in energy dissipation and elastic modulus values are demonstrated in Fig. 7d. The energy dissipation increased from 0.24 to 0.29 MJ m^{-3}, and the elasticity modulus was also increased from 48 to 52 kPa. Compared to pure

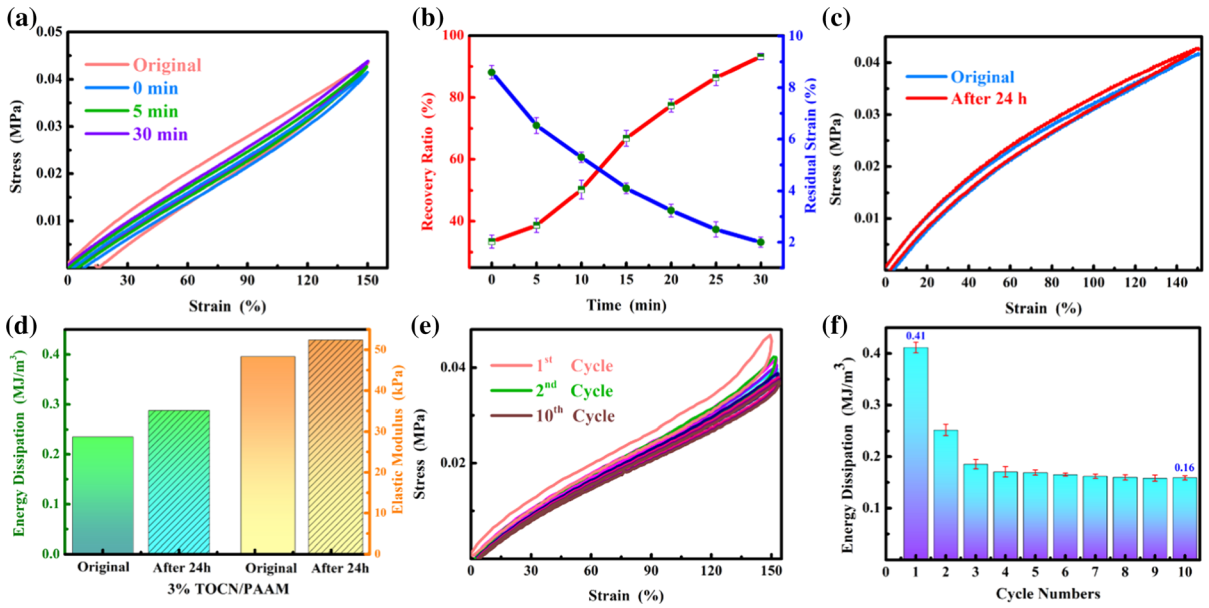

Fig. 7 **a** Cyclic tensile loading–unloading plots and **b** corresponding recovery ratio and residual strain versus time of 3% TOCN/PAAM at 150% strain; **c** cyclic tensile loading–unloading curves of the original and recovered 3% TOCN/PAAM after 24 h resting time, and **d** corresponding energy dissipation and elastic modulus; **e** ten successive cyclic tensile loading–unloading curves of 3% TOCN/PAAM at a strain of 150% without resting between two tests, and **f** corresponding dissipated energy curves

covalently crosslinked PAAM hydrogels, TOCN/PAAM composite hydrogels dissipated a large amount of energy in the cycle test, exhibiting significant hysteresis mainly related to the energy dissipation of hydrogen bond dissociation. After resting for 24 h, the composite hydrogel recovered back to its initial state, and the reversibility of the interfacial hydrogen bonding and crosslinking between the TOCNs and the PAAM was confirmed by the loading–unloading curve which almost overlapped with the initial cycle curve (Yang et al. 2014). After the stress was unloaded, the transient hydrogen bond restored and the network recombined to form a new hydrogel network to alleviate the internal stress of the hydrogel. The occurrence of this self-enhancement phenomenon provided the hydrogel an excellent energy dissipation mechanism.

The 3% TOCN/PAAM composite hydrogel subjected to cyclic tensile loading–unloading test for 10 times at 150% tensile strain showed fatigueless with time interval between two consecutive measurements (Fig. 7e, f). After the first cycle test, the hysteresis loop and the maximum tensile stress of the composite hydrogel were significantly reduced and the dissipated energy value of the second cycle was about 0.25 MJ m^{-3} being approximately 61% of that of the first cycle (0.41 MJ m^{-3}). Continuous damage and deformation caused the internal cross-linking of the hydrogel to break and could not be immediately recovered, resulting in a decrease in tensile strength. However, after 3 cycles, the energy dissipation remained almost unchanged, showing excellent fatigue resistance.

Shape memory behavior

Hydrogels with shape memory function could memorize temporary shapes and restore their original permanent shape through external stimuli (Kahn et al. 2017). The construction of a reversible cross-linking network and the corresponding triggering or conversion methods to impart shape memory properties to hydrogels was a major strategy for the synthesis of shape memory hydrogels (Behl et al. 2010). Since the surface of TOCNs was rich in carboxyl groups, it was easier to form strong coordination bonds with metal ions. Therefore, it could coordinate with metal ions to act as a temporary reversible cross-linking network and prepare the nanocomposite hydrogels with shape memory and adjustable mechanical strength. As

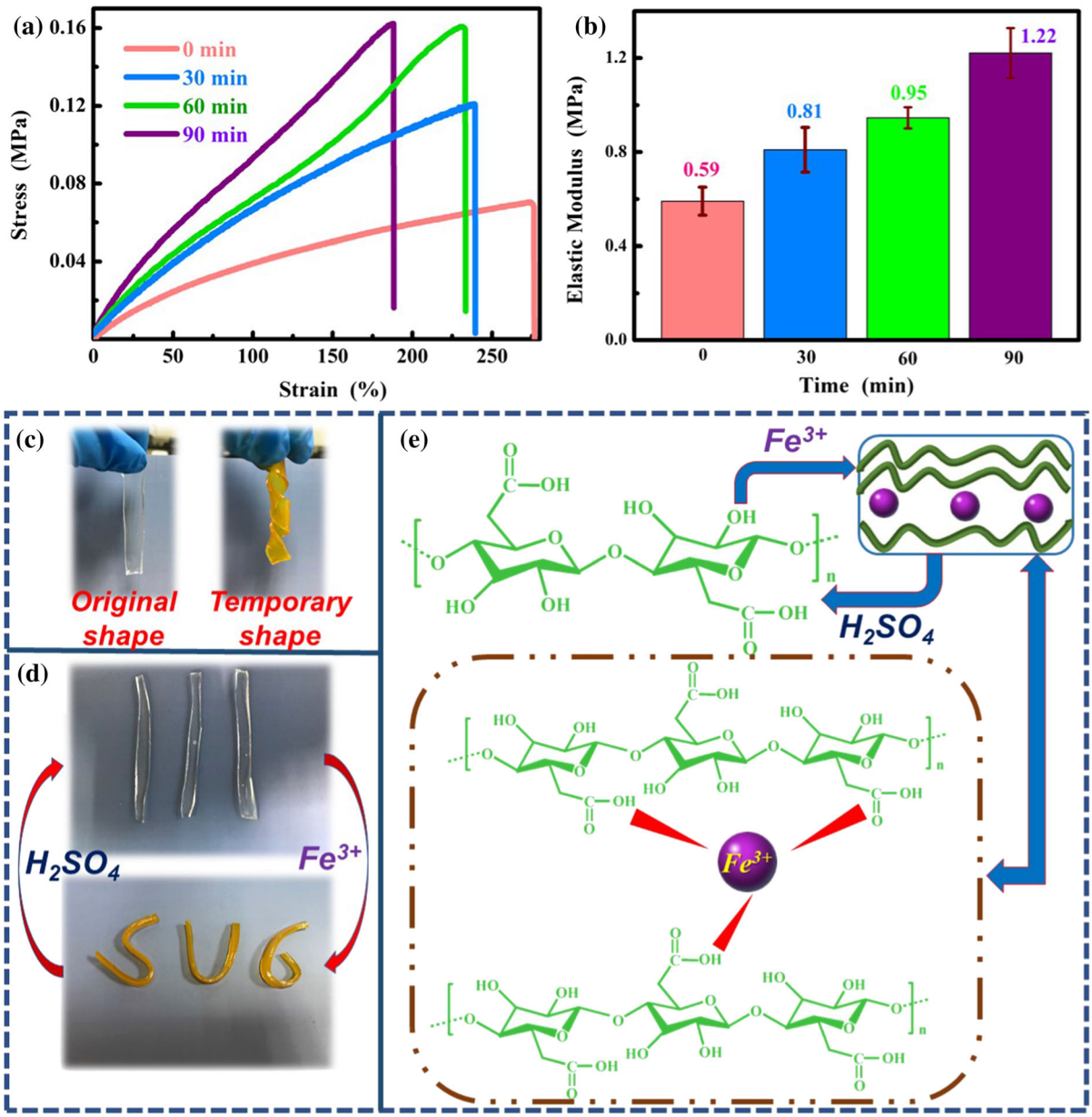

Fig. 8 **a** Tensile stress–strain curves and **b** elastic modulus curves of 3% TOCN/PAAM-Fe^{3+} hydrogels at different immersing durations; **c** original shape and fixed temporary shape in 0.2 M $FeCl_3$ aqueous solution; **d** images of TOCN/PAAM hydrogels fix temporary shapes of "SU6"; **e** schematic illustration of TOCN/PAAM hydrogels in the presence of Fe^{3+}

shown in Fig. 8a, the 3% TOCN/PAAM nanocomposite hydrogel was immersed in a 0.2 M $FeCl_3$ solution adjusting mechanical properties of the hydrogel by changing the different soaking times. With the addition of Fe^{3+}, the interaction between the carboxylic acid groups of TOCNs and Fe^{3+} cations made the internal network of the hydrogel more densely crosslinked which greatly increased the strength and stiffness of the TOCN/PAAM composite hydrogel (Fan et al. 2015). After soaking in $FeCl_3$ solution for 60 min, 3% TOCN/PAAM-Fe^{3+} hydrogel achieved ~ 233% tensile, 0.16 MPa high strength and 0.95 MPa elastic modulus (Fig. 8b). The tensile strength value of the 3% TOCN/PAAM-Fe^{3+}

hydrogel was comparable to that of other previously reported hydrogels (Cong et al. 2014; Gan et al. 2020; Lu et al. 2014; Xu et al. 2019). More importantly, the TOCN/PAAM-Fe^{3+} hydrogel demonstrated shape memory property not found in these articles. When the soaking time in $FeCl_3$ solution increased, the elongation of 3% TOCN/PAAM hydrogel decreased and the elastic modulus increased. After soaking for 90 min in $FeCl_3$ solution, 3% TOCN/PAAM-Fe^{3+} hydrogel achieved ~ 188% of tensile strain, 0.16 MPa of tensile strength and 1.22 MPa of elastic modulus. This was mainly because Fe^{3+} formed coordination interaction with TOCNs. The longer the soaking time, the more Fe^{3+} entered the internal hydrogel, resulting in an increase in the solid content of the hydrogel and a more compact network of enhanced mechanical strength (Li et al. 2017a).

For evaluation of the shape memory behavior of nanocomposite hydrogels under the action of Fe^{3+}, straight hydrogel strips were cut from the prepared 3% TOCN/PAAM hydrogel and twisted into soaked spirals. The shape was fixed in an aqueous solution containing Fe^{3+}, as shown in Fig. 8c, and the hydrogel remained in a spiral state after being taken out from the $FeCl_3$ solution. Since Fe^{3+} had binding affinities for a variety of molecules and anions, many molecules (such as aqueous oxalates, H_2SO_4, carbonate ions, and EDTA) could be used to disconnect the temporary cross-linking of TOCN/PAAM hydrogels with Fe^{3+} and strongly bind to Fe^{3+}, thus endowing TOCN/PAAM-Fe^{3+} hydrogels with excellent shape resilience performance (Li et al. 2017b). The three straight hydrogels were deformed into a "SU6" shape and fixed with Fe^{3+} (Fig. 8d). When immersed in the H_2SO_4 solution, the "SU6" temporary shape was restored to original shape. The possible reaction mechanism was bivalent and trivalent cations such as Fe^{3+} that chelated with TOCNs to stabilize the temporary shape, giving the hydrogel good shape memory properties (Fig. 8e). Therefore, the shape memory effect of the hydrogel was validated in this study, and the shape fixation and shape recovery were achieved and verified by external stimulus changes.

Conclusions

In summary, we reported a TOCN/PAAM nanocomposite hydrogel with intrinsic self-recovery and shape memory performances. Since the hydrogen bond interaction between TOCNs and PAAM chains, the mechanical strength, toughness and fatigue resistance of the hydrogels were significantly improved. The addition of TOCNs also conferred excellent self-recovery property of the hydrogels after mechanical deformation. In addition, the dynamic reversible metal–ligand bonds between Fe^{3+} cations and -COOH groups of TOCNs provided the hydrogel good shape memory properties, and the tensile strength of the hydrogel was greatly improved. Overall, such a composite hydrogel with good shape memory behavior and enhanced mechanical strength can be an attractive candidate for an integrated intelligent system for soft actuators, biomedical and sensory applications. More importantly, this hydrogel platform can be potentially used to prepared organic gels or alcogels by solvent exchange to broaden the scope of their applications.

Acknowledgments Jingquan Han and Ya Lu have contributed equally to this work. This work was funded by National Natural Science Foundation of China (31770609, 31901274), Natural Science Foundation of Jiangsu Province for Outstanding Young Scholars (BK20180090), Qing Lan Project of Jiangsu Province (2019), 333 Project Foundation of Jiangsu Province (BRA2018337), 13th China Special Postdoctoral Science Foundation (2020T130303), China Postdoctoral Science Foundation (2019M661854), Postdoctoral Science Foundation of Jiangsu Province (2019K142), Priority Academic Program Development (PAPD), and Analysis and Test Center of Nanjing Forestry University.

References

Behl M, Razzaq MY, Lendlein A (2010) Multifunctional shape-memory polymers. Adv Mater 22:3388–3410

Bhattacharya A, Misra B (2004) Grafting: a versatile means to modify polymers: techniques, factors and applications. Prog Polym Sci 29:767–814

Chen C, Wang H, Li S, Fang L, Li D (2017) Reinforcement of cellulose nanofibers in polyacrylamide gels. Cellulose 24:5487–5493

Cong H-P, Wang P, Yu S-H (2014) Highly elastic and super-stretchable graphene oxide/polyacrylamide hydrogels. Small 10:448–453

Dai T, Qing X, Wang J, Shen C, Lu Y (2010) Interfacial polymerization to high-quality polyacrylamide/polyaniline composite hydrogels. Compos Sci Technol 70:498–503

Dai X, Zhang Y, Gao L, Bai T, Wang W, Cui Y, Liu W (2015) A mechanically strong, highly stable, thermoplastic, and self-healable supramolecular polymer hydrogel. Adv Mater 27:3566–3571

De France KJ, Hoare T, Cranston ED (2017) Review of hydrogels and aerogels containing nanocellulose. Chem Mater 29:4609–4631

Fan Y, Zhou W, Yasin A, Li H, Yang H (2015) Dual-responsive shape memory hydrogels with novel thermoplasticity based on a hydrophobically modified polyampholyte. Soft Matter 11:4218–4225

Gan D et al (2020) Graphene oxide-templated conductive and redox-active nanosheets incorporated hydrogels for adhesive bioelectronics. Adv Funct Mater 30:1907678

Ge S et al (2020) High-pressure CO_2 hydrothermal pretreatment of peanut shells for enzymatic hydrolysis conversion into glucose. Chem Eng J 385:123949

Ghosh P, Dev D, Samanta A (1995) Graft copolymerization of acrylamide on cotton cellulose in a limited aqueous system following pretreatment technique. J Appl Polym Sci 58:1727–1734

Han J, Lei T, Wu Q (2013) Facile preparation of mouldable polyvinyl alcohol-borax hydrogels reinforced by well-dispersed cellulose nanoparticles: physical, viscoelastic and mechanical properties. Cellulose 20:2947–2958

Han J, Lei T, Wu Q (2014) High-water-content mouldable polyvinyl alcohol-borax hydrogels reinforced by well-dispersed cellulose nanoparticles: dynamic rheological properties and hydrogel formation mechanism. Carbohyd Polym 102:306–316

Han L et al (2018) Mussel-inspired adhesive and conductive hydrogel with long-lasting moisture and extreme temperature tolerance. Adv Funct Mater 28:1704195

Han J et al (2019) A self-healable and highly flexible supercapacitor integrated by dynamically cross-linked electroconductive hydrogels based on nanocellulose-templated carbon nanotubes embedded in a viscoelastic polymer network. Carbon 149:1–18

Hore MJ, Composto RJ (2013) Functional polymer nanocomposites enhanced by nanorods. Macromolecules 47:875–887

Hu J, Zhu Y, Huang H, Lu J (2012) Recent advances in shape–memory polymers: structure, mechanism, functionality, modeling and applications. Prog Polym Sci 37:1720–1763

Hu Y, Du Z, Deng X, Wang T, Yang Z, Zhou W, Wang C (2016) Dual physically cross-linked hydrogels with high stretchability, toughness, and good self-recoverability. Macromolecules 49:5660–5668

Hu Y, Lu C-H, Guo W, Aleman-Garcia MA, Ren J, Willner I (2015) A shape memory acrylamide/dna hydrogel exhibiting switchable dual pH-responsiveness. Adv Funct Mater 25:6867–6874

Huang T, Xu H, Jiao K, Zhu L, Brown HR, Wang H (2007) A novel hydrogel with high mechanical strength: a macromolecular microsphere composite hydrogel. Adv Mater 19:1622–1626

Hynd MR, Turner JN, Shain W (2007) Applications of hydrogels for neural cell engineering. J Biomat Sci-Polym 18:1223–1244

Ivanov A, Larsson H, Galaev IY, Mattiasson B (2004) Synthesis of boronate-containing copolymers of N, N-dimethylacrylamide, their interaction with poly (vinyl alcohol) and rheological behaviour of the gels. Polymer 45:2495–2505

Kahn JS, Hu Y, Willner I (2017) Stimuli-responsive DNA-based hydrogels: from basic principles to applications. Accounts Chemical Res 50:680–690

Kamata H, Akagi Y, Kayasuga-Kariya Y, Chung U-i, Sakai T (2014) "Nonswellable" hydrogel without mechanical hysteresis. Science 343:873–875

Kamphunthong W, Hornsby P, Sirisinha K (2012) Isolation of cellulose nanofibers from para rubberwood and their reinforcing effect in poly (vinyl alcohol) composites. J Appl Polym Sci 125:1642–1651

Khalil HPSA, Davoudpour Y, Islam MN, Mustapha A, Sudesh K, Dungani R, Jawaid M (2014) Production and modification of nanofibrillated cellulose using various mechanical processes: a review. Carbohyd Polym 99:649–665

Kong W, Huang D, Xu G, Ren J, Liu C, Zhao L, Sun R (2016) Graphene oxide/polyacrylamide/aluminum ion cross-linked carboxymethyl hemicellulose nanocomposite hydrogels with very tough and elastic properties. ChemAsian J 11:1697–1704

Kumar SK, Jouault N, Benicewicz B, Neely T (2013) Nanocomposites with polymer grafted nanoparticles. Macromolecules 46:3199–3214

Li C, Mu C, Lin W, Ngai T (2015) Gelatin effects on the physicochemical and hemocompatible properties of gelatin/PAAm/laponite nanocomposite hydrogels. ACS Appl Mater Interfaces 7:18732–18741

Li N et al (2017) Multivalent cations-triggered rapid shape memory sodium carboxymethyl cellulose/polyacrylamide hydrogels with tunable mechanical strength. Carbohyd polym 178:159–165

Li N, Chen W, Chen G, Tian J (2017) Rapid shape memory TEMPO-oxidized cellulose nanofibers/polyacrylamide/gelatin hydrogels with enhanced mechanical strength. Carbohyd Polym 171:77–84

Lin DC, Yurke B, Langrana NA (2004) Mechanical properties of a reversible, DNA-crosslinked polyacrylamide hydrogel. J Biomechan Eng 126:104–110

Liu R et al (2018) Shape memory polymers for body motion energy harvesting and self-powered mechanosensing. Adv Mater 30:1705195

Lu X, Chan CY, Lee KI, Ng PF, Fei B, Xin JH, Fu J (2014) Super-tough and thermo-healable hydrogel–promising for shape-memory absorbent fiber. J Mater Chem B 2:7631–7638

Ma C et al (2018) Bioinspired anisotropic hydrogel actuators with on–off switchable and color-tunable fluorescence behaviors. Adv Funct Mater 28:1704568

Niu J, Wang J, Dai X, Shao Z, Huang X (2018) Dual physically crosslinked healable polyacrylamide/cellulose nanofibers nanocomposite hydrogels with excellent mechanical properties. Carbohyd Polym 193:73–81

Qiu X, Hu S (2013) "Smart" materials based on cellulose: a review of the preparations, properties, and applications. Materials 6:738–781

Saito T, Kimura S, Nishiyama Y, Isogai A (2007) Cellulose nanofibers prepared by TEMPO-mediated oxidation of native cellulose. Biomacromol 8:2485–2491

Saito T, Nishiyama Y, Putaux J-L, Vignon M, Isogai A (2006) Homogeneous suspensions of individualized microfibrils from TEMPO-catalyzed oxidation of native. Biomacromol 7:1687–1691

Salas C, Nypelö T, Rodriguez-Abreu C, Carrillo C, Rojas OJ (2014) Nanocellulose properties and applications in colloids and interfaces. Curr Opin Colloid In 19:383–396

Semenov A, Rubinstein M (2002) Dynamics of entangled associating polymers with large aggregates. Macromolecules 35:4821–4837

Shams Es-haghi S, Weiss R (2017) Do physically trapped polymer chains contribute to the mechanical response of a host double-network hydrogel under finite tensile deformation? Macromolecules 50:8267–8273

Shao C, Chang H, Wang M, Xu F, Yang J (2017) High-strength, tough, and self-healing nanocomposite physical hydrogels based on the synergistic effects of dynamic hydrogen bond and dual coordination bonds. ACS Appl Mater Interfaces 9:28305–28318

Sheng N et al (2019) Polypyrrole@TEMPO-oxidized bacterial cellulose/reduced graphene oxide macrofibers for flexible all-solid-state supercapacitors. Chem Eng J 368:1022–1032

Song J, Tang A, Liu T, Wang J (2013) Fast and continuous preparation of high polymerization degree cellulose nanofibrils and their three-dimensional macroporous scaffold fabrication. Nanoscale 5:2482–2490

Song M-M, Wang Y-M, Wang B, Liang X-Y, Chang Z-Y, Li B-J, Zhang S (2018) Super tough, ultrastretchable hydrogel with multistimuli responsiveness. ACS Appl Mater Interfaces 10:15021–15029

Sun L, Chen W, Liu Y, Li J, Yu H (2015) Soy protein isolate/cellulose nanofiber complex gels as fat substitutes: rheological and textural properties and extent of cream imitation. Cellulose 22:2619–2627

Sun X et al (2020) Carbon nanotubes reinforced hydrogel as flexible strain sensor with high stretchability and mechanically toughness. Chem Eng J 382:122832

Tang C et al (2019) Pickering emulsions stabilized by hydrophobically modified nanocellulose containing various structural characteristics. Cellulose 26:7753–7767

Velichko E, Buyanov A, Saprykina N, Chetverikov YO, Duif C, Bouwman W, Smyslov RY (2017) High-strength bacterial cellulose–polyacrylamide hydrogels: mesostructure anisotropy as studied by spin-echo small-angle neutron scattering and cryo-SEM. Eur Polym J 88:269–279

Wang Y, Chen L (2011) Impacts of nanowhisker on formation kinetics and properties of all-cellulose composite gels. Carbohyd Polym 83:1937–1946

Xia S, Zhang Q, Song S, Duan L, Gao G (2019) Bioinspired dynamic cross-linking hydrogel sensors with skin-like strain and pressure sensing behaviors. Chem Mater 31:9522–9531

Xu J, Jin R, Duan L, Ren X, Gao G (2019) Tough, adhesive and conductive polysaccharide hydrogels mediated by ferric solution. Carbohyd Polym 211:1–10

Yan Y, Wang K, Wang Z, Gindlaltmutter W, Zhang S, Li J (2017) Fabrication of homogeneous and enhanced soybean protein isolate-based composite films via incorporating TEMPO oxidized nanofibrillated cellulose stablized nano-ZnO hybrid. Cellulose 24:4807–4819

Yang J, Han C-R, Duan J-F, Ma M-G, Zhang X-M, Xu F, Sun R-C (2013) Synthesis and characterization of mechanically flexible and tough cellulose nanocrystals–polyacrylamide nanocomposite hydrogels. Cellulose 20:227–237

Yang J, Han C-R, Zhang X-M, Xu F, Sun R-C (2014) Cellulose nanocrystals mechanical reinforcement in composite hydrogels with multiple cross-links: correlations between dissipation properties and deformation mechanisms. Macromolecules 47:4077–4086

Yang J, Han C (2016) Mechanically viscoelastic properties of cellulose nanocrystals skeleton reinforced hierarchical composite hydrogels. ACS Appl Mater Interfaces 8:25621–25630

Yang J, Xu F (2017) Synergistic reinforcing mechanisms in cellulose nanofibrils composite hydrogels: interfacial dynamics, energy dissipation, and damage resistance. Biomacromol 18:2623–2632

Yang R et al (2020a) High capacity oil absorbent wood prepared through eco-friendly deep eutectic solvent delignification. Chem Eng J 401:126150

Yang X et al (2020b) Surface and interface engineering for nanocellulosic advanced materials. Adv Mater 2020:2002264

Yuan N, Xu L, Zhang L, Ye H, Zhao J, Liu Z, Rong J (2016) Superior hybrid hydrogels of polyacrylamide enhanced by bacterial cellulose nanofiber clusters. Mater Sci Eng C 67:221–230

Yue Y, Han J, Han G, French AD, Qi Y, Wu Q (2016) Cellulose nanofibers reinforced sodium alginate-polyvinyl alcohol hydrogels: core–shell structure formation and property characterization. Carbohyd Polym 147:155–164

Yue Y, Wang X, Han J, Yu L, Chen J, Wu Q, Jiang J (2019) Effects of nanocellulose on sodium alginate/polyacrylamide hydrogel: Mechanical properties and adsorption–desorption capacities. Carbohyd Polym 206:289–301

Zhang T, Zuo T, Hu D, Chang C (2017) Dual physically cross-linked nanocomposite hydrogels reinforced by tunicate cellulose nanocrystals with high toughness and good self-recoverability. ACS Appl Mater Interfaces 9:24230–24237

Zhang X et al (2018) Mechanically robust and highly compressible electrochemical supercapacitors from nitrogen-doped carbon aerogels. Carbon 127:236–244

Zhao D, Zhu Y, Cheng W, Chen W, Wu Y, Yu H (2020) Cellulose-based flexible functional materials for emerging intelligent electronics. Adv Mater 2020:2000619

Zhao D et al (2020) A dynamic gel with reversible and tunable topological networks and performances. Matter 2:390–403

Zhao X (2014) Multi-scale multi-mechanism design of tough hydrogels: building dissipation into stretchy networks. Soft Matter 10:672–687

Zheng C et al (2020) A stretchable, self-healing conductive hydrogels based on nanocellulose supported graphene towards wearable monitoring of human motion. Carbohyd Polym 250:116905

Zhou C, Wu Q, Yue Y, Zhang Q (2011) Application of rod-shaped cellulose nanocrystals in polyacrylamide hydrogels. J Colloid Interf Sci 353:116–123

Zuluaga R, Putaux JL, Cruz J, Vélez J, Mondragon I, Gañán P (2009) Cellulose microfibrils from banana rachis: Effect of alkaline treatments on structural and morphological features. Carbohyd Polym 76:51–59